Hindawi
Advances in Civil Engineering
Volume 2023, Article ID 8871629, 17 pages
https://doi.org/10.1155/2023/8871629

Research Article

Particle Swarm Optimization of Support Vector Machine Inversion Model for Overhead Upright Piers Damage-Inducing Factor

Shiliang Zhou, Menghan Tang, Jun Wu, and Chunru Ke

Southwest Research Institute for Hydraulic and Water Transport Engineering, Chongqing Jiaotong University, Chongqing 400074, China

Correspondence should be addressed to Menghan Tang; 622210090056@mails.cqjtu.edu.cn

Received 5 July 2023; Revised 13 November 2023; Accepted 16 November 2023; Published 13 December 2023

Academic Editor: Giovanni Garcea

In the Three Gorges reservoir area, the overhead upright pier is the primary structural form. For intelligent monitoring of existing terminals, this research chooses Chongqing Xintian Port as the study object and proposes a support vector machine (SVM) damage-inducing factor (DIF) inversion model based on particle swarm optimization (PSO). To apply the finite element method to analyze the stress distribution characteristics of quay pile groups under three main DIFs, including the stacking effect, ship impact load effect, and bank slope effect. After characterizing the stress data, it becomes evident that there exists a correlation between stress and each DIF parameter. Before generating the training sample set, principal component analysis is employed to reduce dimensionality and eliminate a substantial amount of redundant data. The model has an accuracy of 0.999 for the identification of the type of DIF and 0.975 for the identification of the location of the action of the DIF with $F1$ coefficients of 0.999 and 0.978, respectively. For the strength of DIF predictions, MAE and MSE were 4.871 and 1.202, respectively, R^2 was 0.986, NSE was 0.986, WI was 0.996, and PBIAS was 0.095. After extracting every sample, the relative error for the ship impact load effect is 0.05, and the highest relative error for the bank slope effect is 0.02; the error for the stacking effect is limited to 0.08. The results suggest that the damage inducement inversion model of the SVM optimized by the PSO algorithm can effectively identify the DIF of the overhead upright pier.

1. Introduction

Overhead upright wharf has the advantages of adapting to large water level variation, good berthing stability, and high loading efficiency, and is widely used in the construction of the quay in the Three Gorges reservoir [1]. However, the long-term and continuous loading makes the wharf structure prone to damage, so real-time monitoring of the load and timely control of damage has become a key guarantee of the long-term reliable operation of the wharf.

The existing technology for monitoring the health of the wharf mainly focuses on the identification and localization of damage after it has occurred, monitoring structural deformations, and conducting external inspections of the wharf [2, 3]. For example, Huang and Wei [4] proposed methods for external inspections, including rust monitoring. Zhao et al. [5] established damage identification indicators based on structural dynamic responses. These scholars mainly focus on monitoring mechanical parameters and deformations of wharf structures after damage has occurred, but they pay less attention to the monitoring and intervention of loads before damage occurs. Therefore, this study introduces the concept of the "Damage-Inducing Factor" (DIF) and incorporates load monitoring indicators into the monitoring of overhead vertical dock structures. We aim to advance research on damage inducement, to detect potentially dangerous loads promptly at the early stage of load application, before damage occurs, and to take necessary intervention measures.

"Damage-Inducing Factor" is defined as the application of loads to structures that exceed regulatory limits but do not cause damage to the dock. It serves as a "yellow light" warning for dock operations. Therefore, monitoring and analyzing

damage inducement are essential components of load monitoring. During the operation of docks, adverse factors such as overloading, reckless berthing of ships [6, 7], and lateral soil pressure on the shore slope often lead to structural damage. Hence, we have selected these three main detrimental factors as the focus of our research.

Pile foundations are the most critical load-bearing components of dock structures and provide an important window for observing the structural load state. Therefore, the study of the "Damage-Inducing Factor" aims to establish a nonlinear mapping between the mechanical characteristics of pile foundations and the load state of the entire dock structure, enabling the reverse calculation of structural load state from pile foundation stress.

For the issue of nonlinear mapping mentioned above, machine learning offers unique advantages. For instance, Shu et al. [8] used various models to identify the stability of slopes. Wang et al. [9] employed Support Vector Machines (SVM) to assess the factors influencing the thermal deformations of dams and explained the impact of temperature on deformations. Li et al. [10] used the Differential Evolution Grey Wolf Optimization-SVM to predict the real displacement of dam bodies. SVM, as a classic machine-learning model, performs well in high-dimensional data and exhibits excellent generalization capabilities, especially for small-sample data [11]. However, SVM's performance is closely related to kernel parameters and penalty factors [12], which, to some extent, limits its application. Particle swarm optimization (PSO) has a fast convergence rate and fewer hyperparameters, making it a popular choice for optimizing hyperparameters [13–16]. For example, Jia et al. [17] combined PSO with locally supported SVM and used PSO to optimize parameters for landslide prediction. Fei et al. [18] introduced the PSO algorithm to estimate the permeability coefficient of engineering rock and soil non-watertight structures based on PSO–SVM. Hence, PSO has been selected as the optimization technique for SVM.

To meet the demand for real-time monitoring of overhead upright quay structure, this research takes Chongqing Xintian Port as the research object and uses the finite element method to analyze its static monitoring index under the effect of damage inducements such as stacking effect, ship impact load effect, and bank slope effect. This research proposes an SVM inversion model based on the PSO algorithm, which can identify the idiosyncrasies of the stress distribution in the pier pile foundation and perform real-time monitoring and early warning work on the damage inducement of overhead upright piers. This study can provide technical references for the safe operation of the wharf.

2. Group Piles in Overhead Upright Piers under the Influence of DIFs: Stress Analysis

2.1. Model Building and Material Parameters Selection. The structural section 8 of the first phase of the Xintian Port in Chongqing is used as a general research object, and a finite element model is established, as shown in Figure 1, to completely constrain the bottom surface and to constrain the normal displacements of the four bedrock sections in the front, back, left, and right. The normal displacements on the side and rear of the bank slope are restricted in the initial stage. When the bank slope effect is loaded after the balancing of in situ stress, the restriction on the displacement behind the bank slope is released. The model uses C3D8R solid elements, which have a total of 42,481 units and 542,485 nodes. Table 1 is used to determine the material properties.

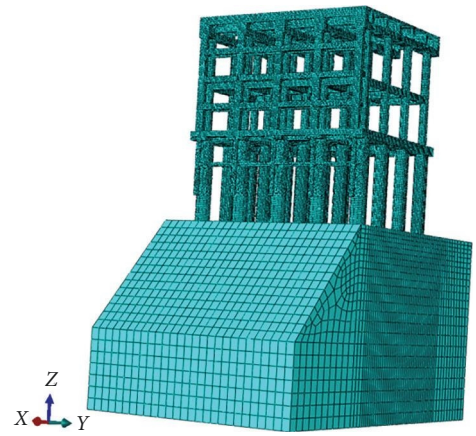

Figure 1: Finite element model of the wharf.

2.2. DIFs. DIFs are actions taken on the quay structure that exceed the quay code value but does not result in the quay structure failing from overload action. As a quay monitoring indicator, DIFs are the quay components before the emergence of the "yellow light" stage of plastic damage. By monitoring the DIFs, companies possess the ability to carry out berthing optimization, shore monitoring, and other control operations in advance to stop the damage at its source and stop it from getting worse.

The DIF working conditions are taken according to the Chinese "JTS144-1-2010", "JTG D60-2015," and "GB50007-2011," and the design values are enlarged appropriately (by 20%–50%). Due to the large transverse stiffness of the quay, the shipload only considers the force perpendicular to the frontier line of the quay. Specific values are taken, as shown in Table 2.

The stacking effect position is shown in Figure 2, and the stacking area of the quay panel is divided into four blocks. The ship impact load effect position is shown in Figure 2, and 15 impact positions are set according to different water levels. The bank slope effect mode is shown in Figure 2, and the load is equated to the surface load. According to Table 2, three groups of different DIFs were selected for calculation; Group I applied a 30 kPa uniform load in area 3, and Group II applied a 500 kN equivalent static ship impact action on the 3-bay row frame three berthing members. Group III applied a shore slope action of 1,200 kN.

2.3. Group Pile Stress Distribution Characteristics Analysis. Figure 3 displays the outcomes of the calculation for Group I. For real-time wharf monitoring, stress collection points are placed between the design low water mark (143.6 m) and the top of the pile (153.4 m), with five stress collection points

Table 1: Material parameters.

Material category	Density (kg/m^3)	Young modulus (Pa)	Poisson ratio	Internal friction angle (°)	Cohesion (kPa)	Expansion angle (°)
Reinforced concrete	2,500	3.0×10^{10}	0.25	–	–	–
Steel member	7,850	2.06×10^{11}	0.3	–	–	–
Riprap compaction	2,300	2.5×10^{10}	0.25	37	5	0.1
Bedrock	2,400	2.2×10^{10}	0.21	32	150	0.1

Table 2: Work conditions of damage-inducing factors.

	Damage-inducing factors	Point	Direction	Strength of effect
1	Stacking effect and gravity	Panel #1–4	Vertical downward	10–55 kPa
2	Ship impact load effect and gravity	Berthing member #1–15	Horizontal toward the shore side	150–600 kN
3	Bank slope effect and gravity	Back side of soil	Horizontal toward the river side	0–1,300 kN/m

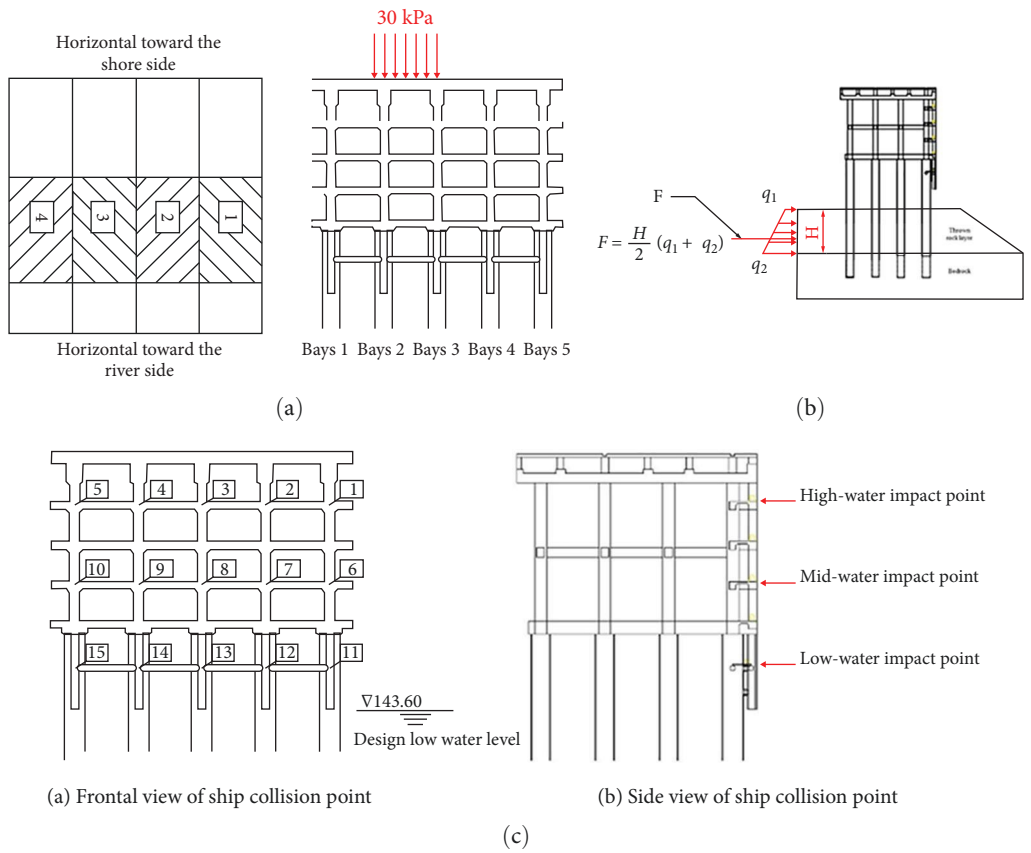

Figure 2: Method of lateral earth pressure of slope: (a) illustration of stacking effect; (b) illustration of bank slope effect; (c) illustration of ship impact load effect.

placed at equal intervals from top to bottom for each pile. The locations of these 20 pile bases and 100 collection points are depicted in Figure 4. Each pile foundation's stress collecting locations are labeled no. 1 (top), no. 2, no. 3, no. 4, and no. 5 (bottom), in that order.

The stress data at the collecting location of each pile foundation 1 are displayed as indicated in Figure 5(a)–5(c), which was created by extracting the calculation results of the three groups of working circumstances defined in the previous section. As seen in Figures 5(a) and 5(c), the horizontal stresses caused by the stacking effect and the bank slope effect are distributed among the piles in an arch-like pattern, with the stacking effect stress concentrations being higher at the second and third rows of piles and the bank slope effect concentrations being higher at the bases of the fourth row of piles and gradually decreasing toward the riverside. From

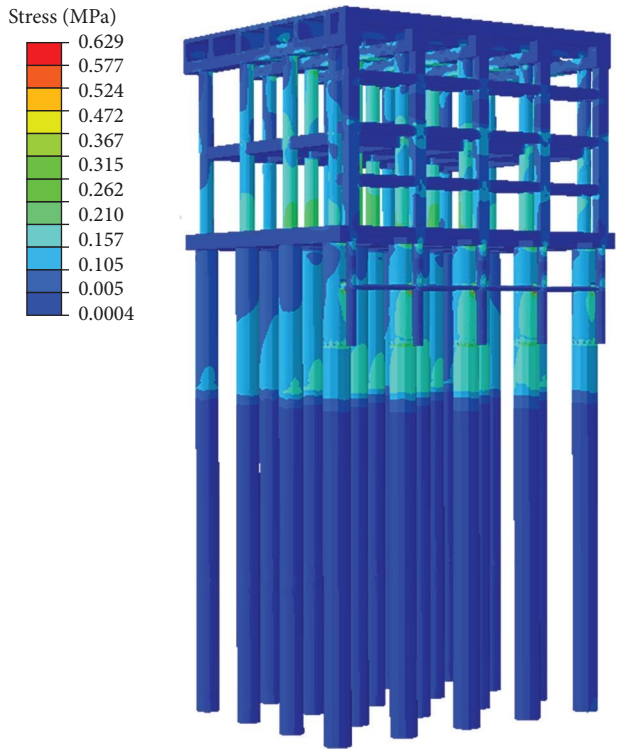

Figure 3: Stress program under stacking load in no. 3 stacking load area.

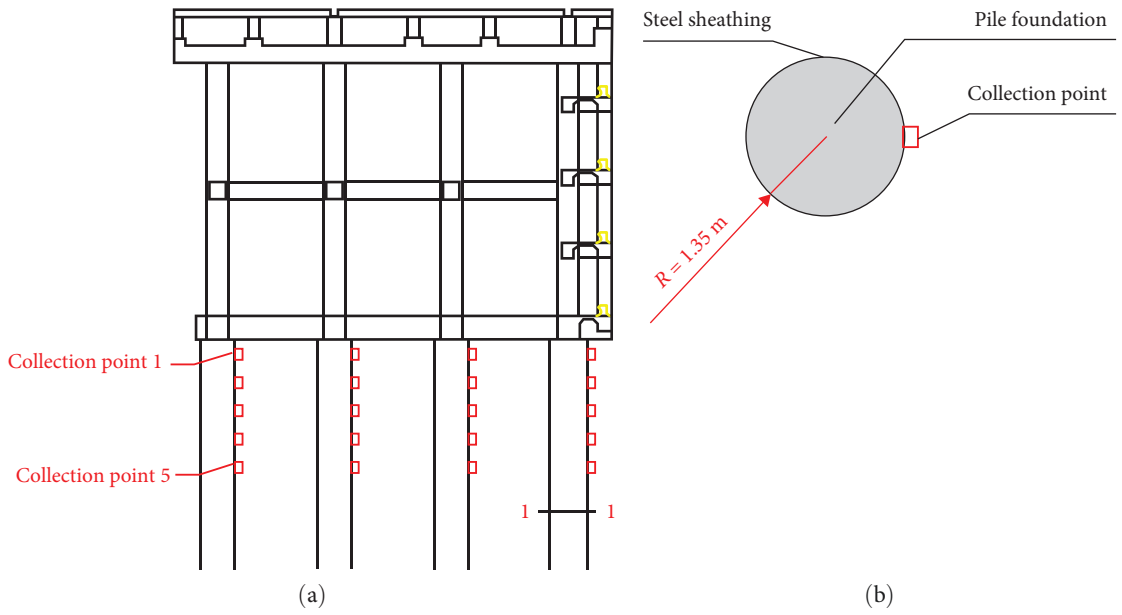

Figure 4: The layout of stress acquisition points: (a) side view of pier; (b) 1–1 cross-section.

Figure 5(b), it is clear that the horizontal stress at the front row of the piling foundation's collecting point beneath the impact position (impact point no. 3), which is subject to the effects of ship impact loads, changes abruptly. Due to the intricate coupling effect of the quay superstructure, the impact on the last three rows of pile foundations is less severe. As seen in Figure 6(a)–6(c), the stress data from each collecting point of the first row of the pile foundation are plotted. It is discovered that the vertical stress of the pile foundation shows a more pronounced progression with location and that the pattern of distribution under the influence of each damage inducement should differ.

The above investigation reveals that the group pile stress distribution exhibits clear specificity when subjected to various

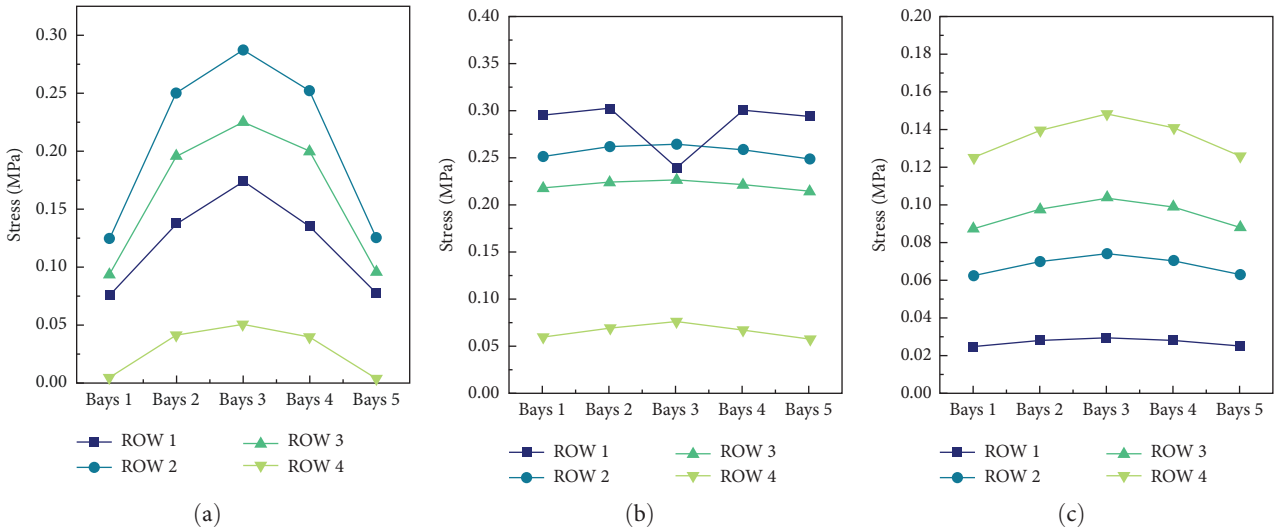

Figure 5: Horizontal stress distribution at group pile collection points: (a) stacking effect; (b) ship impact load effect; (c) bank slope effect.

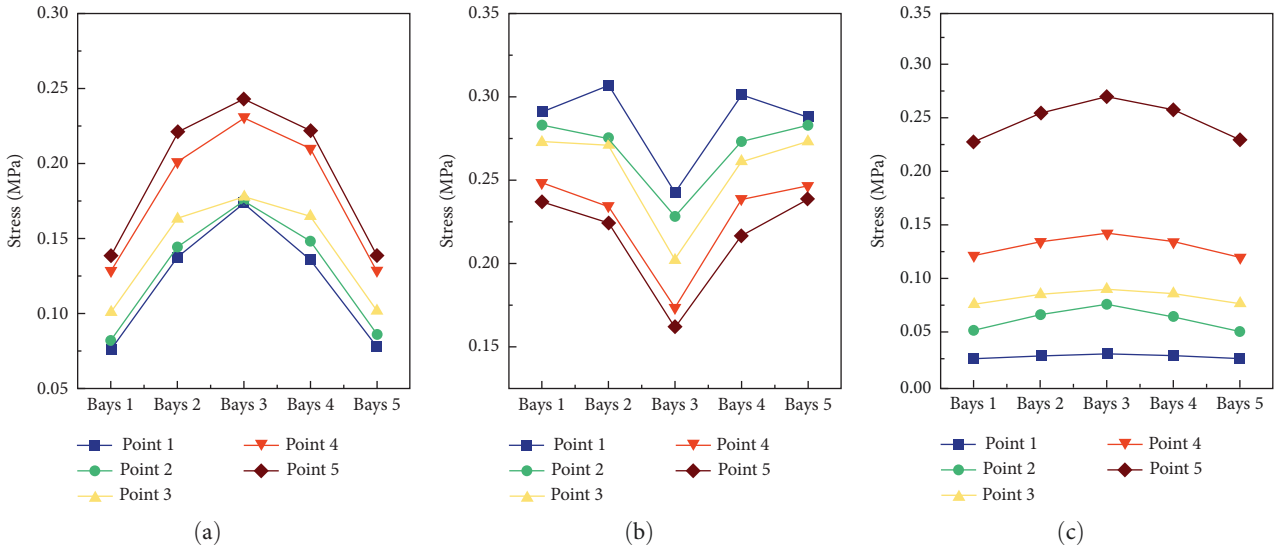

Figure 6: Vertical stress distribution at group pile collection points: (a) stacking effect; (b) ship impact load effect; (c) bank slope effect.

damage inducements, which can offer feature values for the inverse identification of damage inducement.

3. Inducement Inversion Model Based on PSO–SVM

3.1. SVM-Based Inversion Model for Damage Inducement. Based on the stress data at known collection places, damage inducement inversion seeks to precisely determine the type, location, and intensity of damage inducement on the wharf structure. The inversion of its intensity is a nonlinear regression problem, while the identification of its location and type of action is a classification problem [19].

SVMs employ rigorous optimization theory and mathematical reasoning to provide a singular response to this question [20]. SVMs, as opposed to neural networks, offer the benefit of eliminating structural risk, solving problems without local extrema, and also having strong generalization performance with small samples and the ability to accurately estimate any function [21]. So, a mathematical model for damage inducement inversion based on SVMs is suggested in this study.

$$\begin{cases} Y^{pr} = SVM(X) \\ Y^{pr} = \left(y_1^{pr}, y_2^{pr}, y_3^{pr}\right), \\ X = (x_1, x_2, x_3 \ldots x_l) \end{cases} \tag{1}$$

where Y^{pr} represents the target vector to be inverted. y_1^{pr}, y_2^{pr}, y_3^{pr} represents the inverse damage inducer type, action location, and action intensity, respectively. X represents the reduced dimensional strain vector. l represents the dimensionality of X.

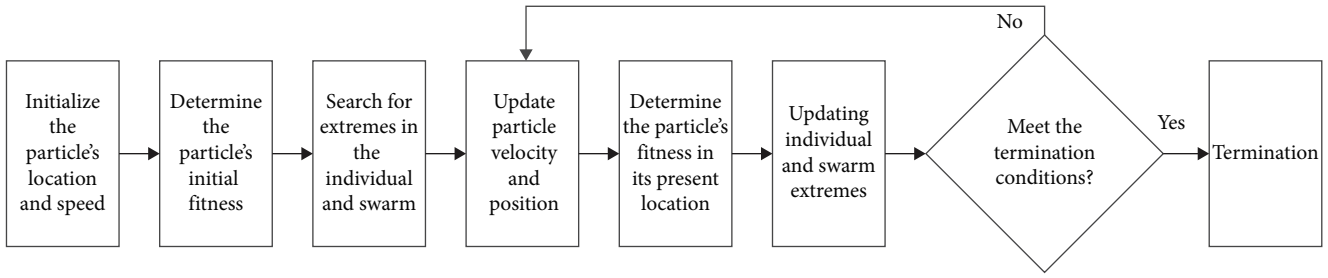

Figure 7: Flowchart of particle swarm optimization algorithm.

The original challenge of resolving the damage-causing component Y is represented by the distribution of sample points in space after the model imports the inverse samples. The original issue is changed into a related dyadic problem using quadratic convex optimization theory. The dyadic problem is then solved using the SMO method to get the globally optimal decision plane, which completes the inversion of the DIF. The kernel function is introduced to map the sample points to higher dimensions for the nonlinear issue. The use of Gaussian kernel functions to handle nonlinear samples has been demonstrated in studies [22] to have a high level of accuracy. The use of the Gaussian kernel function is made in this research.

$$\kappa(X_i, X_j) = \exp\left(-\frac{\|X_i - X_j\|}{2\sigma^2}\right), \tag{2}$$

where σ represents the bandwidth of the Gaussian kernel. x_i, x_j represents the sample vectors.

3.2. Optimization Solution Based on PSO. The correctness of the mathematical model is significantly impacted by the SVM's σ bandwidth and the penalty factor C Composed during the solution process, according to studies [21], and establishing the parameter values by trial calculations has a significant blind spot.

PSO [23, 24] is introduced in this research. Each particle in this algorithm represents a potential solution, and its position reflects the fitness value the fitness function determined. To achieve the overall optimization, the movement of the particles is dynamically changed by other particles' movement experiences. Its convergence speed is rapid, and its computational volume is less than that of the genetic algorithm. The optimal SVM in this work contains only two hyperparameters, yet its sensitivity is great and significantly affects the outcomes. The PSO algorithm is chosen because it has a fast convergence speed, a strong global search, and a relatively simple structure. Manually adjusting the parameters results in a large workload and low accuracy, while the other optimization methods introduce more hyperparameters to make the model more bloated. Figure 7 displays the optimization's flow.

The fitness function for the inverse identification of the damage-inducing agent's mode and site of action is as follows:

$$k_i = \begin{cases} 1, y_i \neq y_i^{pr} \\ 0, y_i = y_i^{pr} \end{cases}, \tag{3}$$

$$fit_c = \sum_{i=1}^{n} k_i, \tag{4}$$

where y_i represents the true damage inducement type and location of the action, y_i^{pr} represent the damage inducement type and location of the effect of counter-performance and n represents the number of samples.

The fitness function for the inversion of the strength of the DIF's effect is as follows:

$$fit_r = \frac{1}{n}\sum_{i=1}^{n} \left\|S_i - S_i^{pr}\right\|_2^2, \tag{5}$$

S_i represents the true damage inducement effect intensity, S_i^{pr} represents the damage inducement effect intensity of the counter-performance, and n represents the number of samples.

4. Construction of Inverse Sample Set for Damage Inducement

4.1. Batch Processing of Finite Elements Method Calculations. Python is utilized for the secondary development of finite element software to implement batch finite element model solution calculation and batch result extraction. The steps are shown in Figure 8.

The experimental batch calculates 10,000 sets of stacking action conditions, 10,000 sets of ship impact action conditions, and 1,000 sets of shore slope action conditions. Finally, the stress data at their collection points are extracted accordingly.

4.2. Sample Data Analysis. Box line diagrams, as shown in Figure 9(a), were created by extracting the single-dimensional stress data under various impact point locations. The box line diagrams, from bottom to top, represent the minimum, first quartile (Q1), median, second quartile (Q2), and maximum values of the data, respectively, and show the distribution characteristics of the data. Figure 9 shows that the stress data appear to have a clear regularity with the impact point location, the impact point from right to left (1–5/6–10/11–15), and the stress at this monitoring point will increase

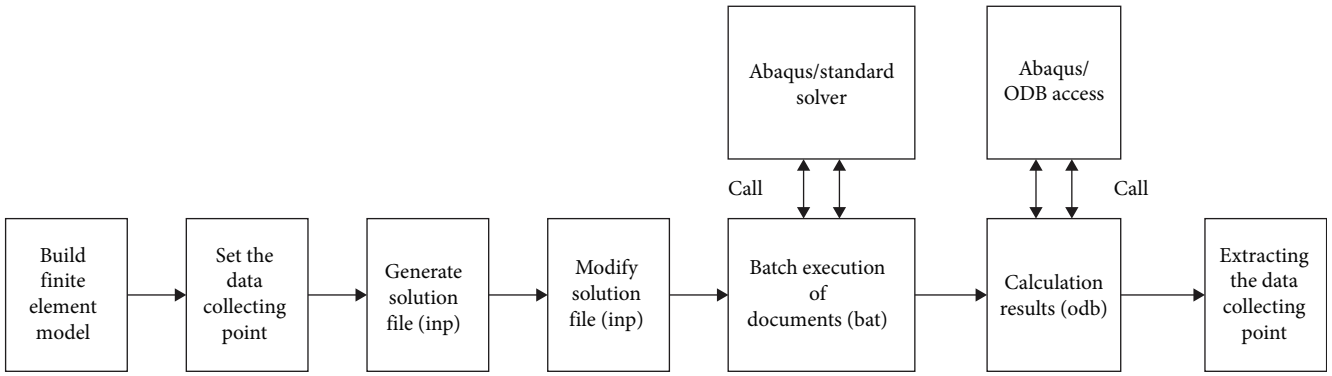

Figure 8: Batch processing flow.

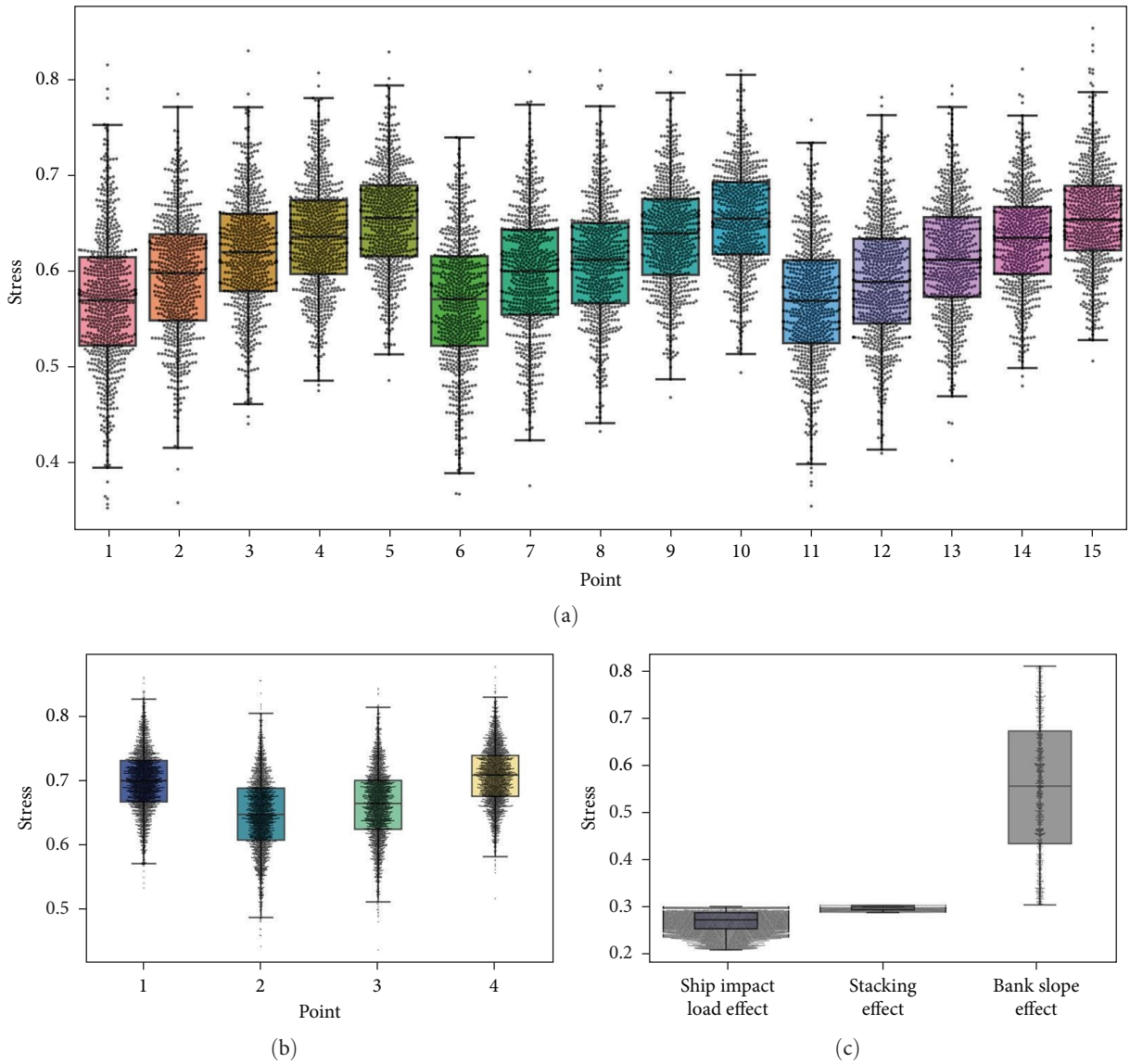

Figure 9: Stress box line diagram of stress: (a) position of ship impact load effect; (b) position of stacking loading; (c) types of damage inducements.

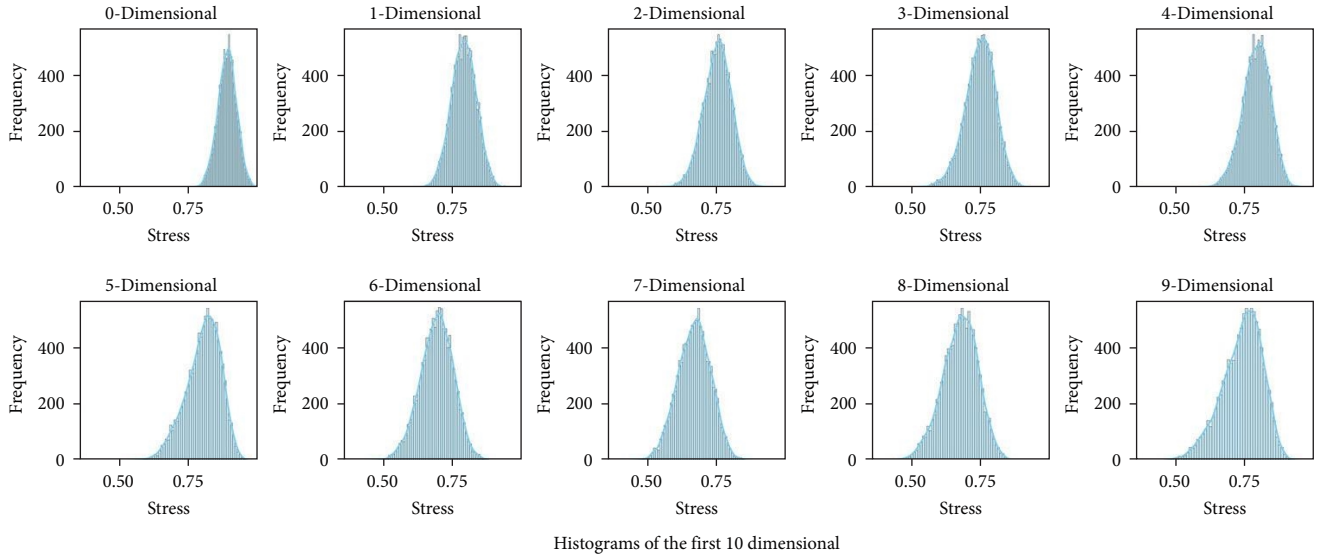

FIGURE 10: Histogram of stress in the top 10 dimensions.

significantly. Box line diagrams, as shown in Figure 9(b), are created by extracting the single-dimensional stress data under various pile load locations. The stress distribution is also correlated with the stacking position.

Stresses for different DIF categories were extracted and plotted as in Figure 9(c). The stress levels under various damage inducer types range significantly from one another. Out of the three, the pier slope action has the potential to cause the floating greater strains on the pier piles, perhaps resulting in a more dangerous pier structure.

The location and kind of DIF are strongly correlated with the stress data, as seen by all of the aforementioned figures. The rich feature information in the stress data may be utilized as the model eigenvalues.

The stress data for the first 10 dimensions were extracted to plot a histogram as in Figure 10. Although the dimensional stress data shows some minor variations, the overall distribution remains constant, indicating that there are redundant data points and a lot of information features. As a result, the dimensionality reduction process must be completed.

4.3. Construction of the Inverse Sample Set. To extract meaningful information, the stress data that were retrieved above must be downscaled. Principal component analysis (PCA) [21] is frequently used to process data that have been dimensionally reduced. The general steps for PCA processing are as follows:

Hypothetical data sample $T = (\alpha_1, \alpha_2, \alpha_3, \ldots \alpha_m)$, m is the number of samples, and the dimension of each sample is n. The covariance matrix C is calculated by Equation (6).

$$C = \frac{1}{m-1} \sum_{j=1}^{m} \left(\alpha_j - \overline{\alpha}\right)\left(\alpha_j - \overline{\alpha}\right)^T, \tag{6}$$

where the $\overline{\alpha}$ represents the mean of the sample, and then the feature value λ and its corresponding feature vector U are calculated by solving Equation (7).

$$(\lambda I - C)U = 0, \tag{7}$$

where I represents the unit matrix such that $\lambda_1 > \lambda_2 > \ldots > \lambda_m$ and their corresponding feature vectors are $U_1, U_2, \ldots, U_m$. The transformation matrix W formed by them as follows:

$$W = [U_1 U_2 \ldots U_m], \tag{8}$$

Calculate the final PCA transformation from W:

$$Y = W^T T, \tag{9}$$

where Y represents the altered data. Typically, the most useful information is found in the first r rows of Y. Therefore, to achieve data dimensionality reduction, the first r rows are extracted. r Select by the following formula:

$$\frac{\sum_{j=1}^{r} \lambda_j}{\sum_{j=1}^{m} \lambda_j} \geq 0.95. \tag{10}$$

As a result, the sample's dimensionality is decreased from n to r dimensions while still retaining more than 95% of the informational value of the original data sample.

The data normalization is done by the following equation:

$$T_i' = \frac{\alpha_i - \alpha_{\min}}{\alpha_{\max} - \alpha_{\min}}, \tag{11}$$

where T_i' represents the normalized sample, $\alpha_{\max}$, $\alpha_{\min}$ represents the maximum and minimum values in the sample.

Table 3: Dimensions and information content after data processing.

Data processing method	Data dimension	Data information content (%)
Raw data	100	100
Normalization process	100	100
PCA	23	95.7

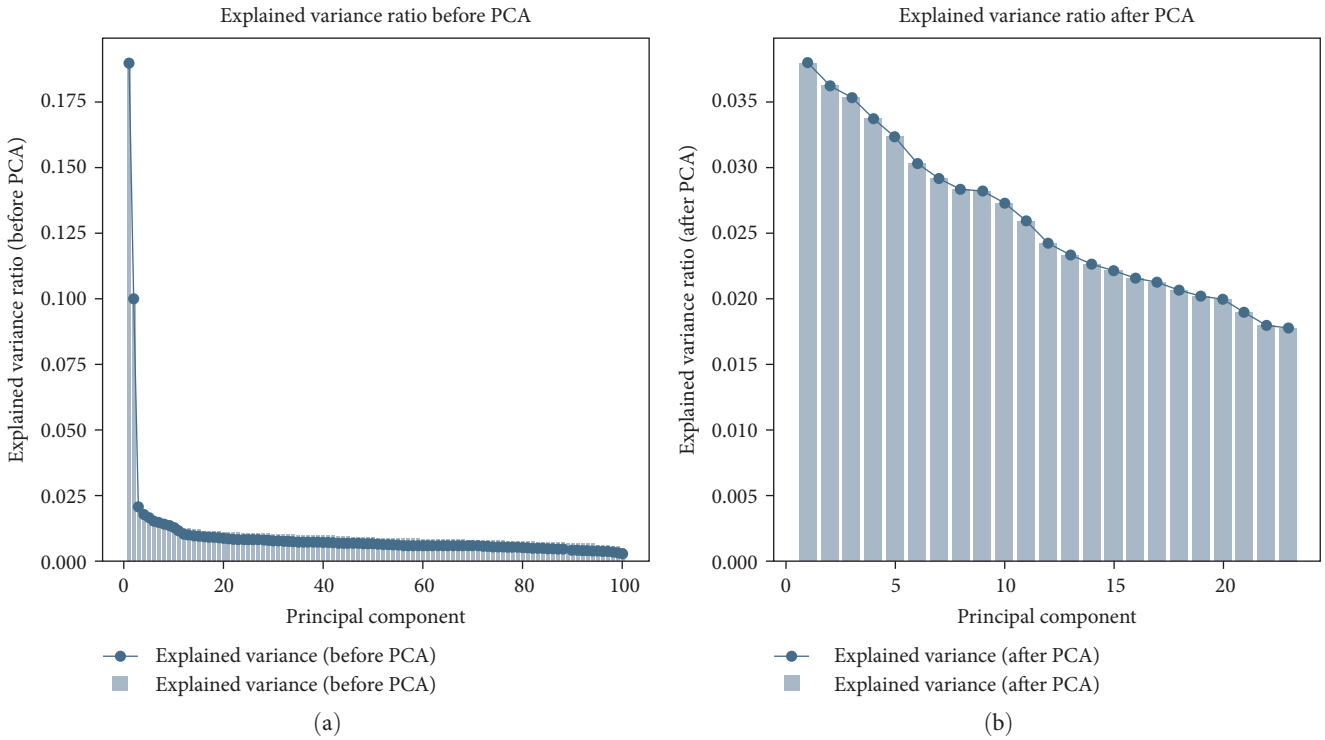

Figure 11: Interpretable variance of data before and during reduction of dimensionality: (a) pre-dimensionality; (b) after dimensional reduction.

After normalization and dimensionality reduction, the number of dimensions and the information content of the data are shown in Table 3.

Figure 11 displays the plot of the interpretable variance of stress data before and after dimensionality reduction. Figure 11 illustrates how there was a significant variation in the percentage of interpretable variance between the stress data before and after dimensionality reduction. While some stress data accounted for a high percentage of interpretability, others had a very low percentage. Following dimensionality reduction, the data's percentage of interpretable variance became more uniform, indicating that each dimension's relative importance had increased and that no major dominant feature of the stress data was present in any one dimension. This indicates that PCA removes some duplicate data while extracting a great deal of valuable information.

The inverse sample's feature X_d is constructed from the reduced-dimensional stress data, where the number of rows in X_d corresponds to the sample's number and the number of columns to its dimension. With the number of lines equaling the number of samples, denote y_1, y_2, y_3 as the various types, locations, and strengths of damage induction. The sample set for the inversion of damage inducement is recorded as a matrix with the columns X_d, y_1, y_2, y_3.

5. SVM Damage Inducement Inversion for PSO

5.1. DIF Inversion Procedure Based on PSO–SVM Model. Figure 12 plots the overall research framework and the inversion process, which includes data characterization, model accuracy analysis, and the construction of the PSO–SVM inversion model.

5.2. Optimization Training of Inverse Model. The 21,000 datasets in the generated inverse sample set were randomly chosen as 80% of the training sample set and 20% of the test sample set for the optimization training of the inverse model. Figure 13 illustrates the iterative process of parameter optimization for the SVM inverse model using the particle swarm technique. The model tends to converge after a predetermined number of iterations.

The particle swarm algorithm hyperparameters are set in Table 4. The number of particle swarms is represented by swarm size in Table 4, the maximum number of iterations is represented by Maxiter, the upper and lower limits of the

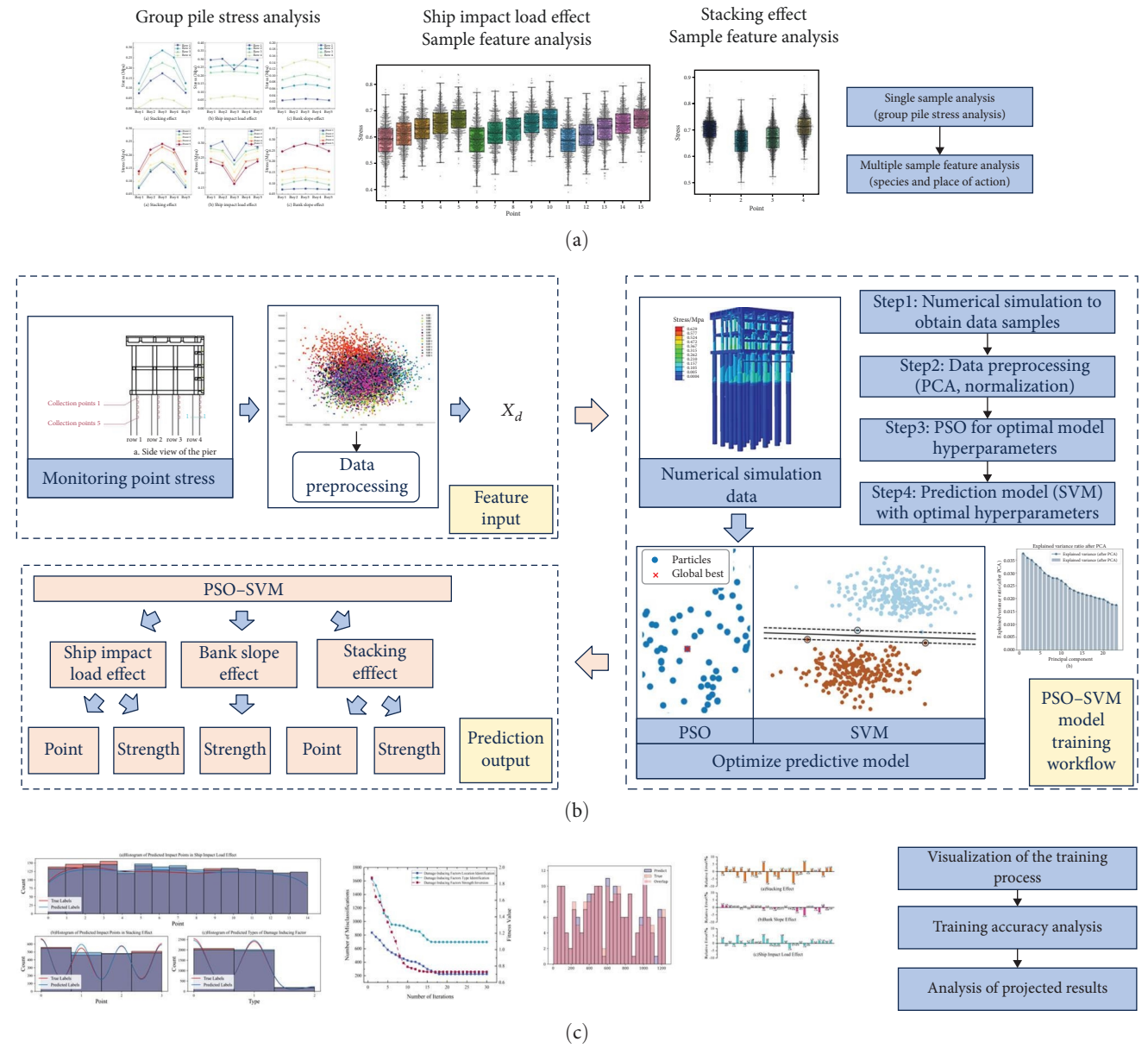

FIGURE 12: Research framework: (a) sample feature analysis; (b) prediction workflow of damage-inducing factors inversion model based on PSO–SVM; (c) analysis of model prediction accuracy.

particle search are represented by lb and ub, and the optimal hyperparameters for particle swarm search are best_C, best_gamma.

The performance of the categorical inverse model for damage inducement types and action locations on the training sample set after optimization is shown in Table 5.

The regression inversion model of the damage inducement strength was optimized, and the realizations on the training sample set are shown in Table 6.

In Table 5, precision indicates the proportion of the number of correctly predicted samples in the sample set to the total number of samples. The higher the value, the better the sensitivity of the model. $F1$-score is the summed average of precision and recall, and the larger the value, the higher the sensitivity and precision of the model. The above three values range from 0 to 1, and the closer the value is to 1, the better the generalization ability of the model. After the optimization of the inverse model for DIF type and action location, the above three indexes are above 0.978, indicating that the optimized inverse model has high sensitivity and accuracy in the training sample set.

In Table 6, the mean absolute error (MAE) and mean squared error (MSE) represent the degree of difference between the predicted and true values of the model, which is calculated in the following equations [25]:

$$MAE = \sum_{i=1}^{n} \left| y_i - y_i^p \right|, \tag{12}$$

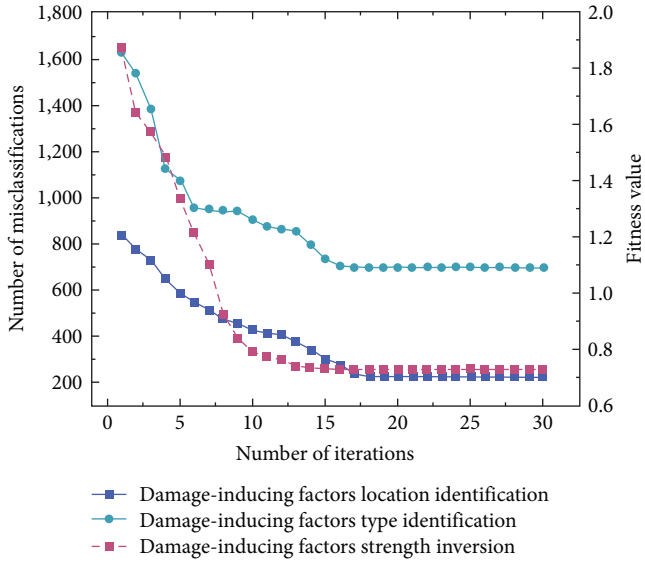

Figure 13: Particle swarm optimization iteration process.

Table 4: Particle swarm hyperparameter.

Hyperparameter	Swarm size	Maxiter	lb	ub	Best_C	Best_gamma
	50	30	0.1	50	6.153	0.598

Table 5: Classify model training metrics.

Inversion category	Sample size	Precision rate	*F*1-score	Recall rate
Types of damage inducement effect	16,800	0.999	0.998	0.996
Location of damage inducement effect	16,800	0.979	0.978	0.978

Table 6: Regression model training metrics.

Inversion category	Sample size	MAE	MSE
The strength of damage-inducing factor	16,800	2.488150	0.731

$$MSE = \sum_{i=1}^{n} \left(y_i - y_i^p\right)^2. \tag{13}$$

5.3. Classification Prediction by Inverse Model of Damage Inducement Factor Types and Location. The machine-learning model must not only perform well on the training sample set but also be able to recognize and predict sample points outside of the training sample, i.e., the model must not be overfitted and have good resilience. The predictions of the type and location of damage inducement were then projected as a heat map, and the inverse model was tested using the test sample set created in the previous section. The test sample set's model performance is indicated in Figure 14 and Table 7 for the model.

Comparing Table 5 with Table 7, the three indices of the model decreased slightly, but their values were still above 0.975. In summary, the inverse model has an excellent performance in the test sample set for the inverse identification of the type and location of damage inducement, which proves that the model does not have the phenomenon of overfitting and has good robustness.

The numbers in Figure 15's diagonal represent how many test sample sets the inversion model accurately predicted. For instance, the first row of Figure 15(a) shows that, of the 2007 test sample sets for the stacking action, 2006 sets were correctly predicted by the inversion for the type of damage causation, and one set was mistakenly identified as shore slope action. The values in the classification model that are on the diagonal are all significantly greater than the other values.

Plotting the predicted structure of the injury causative agent type and the location of action as a histogram, as shown in Figure 16, and adding the kernel density curve

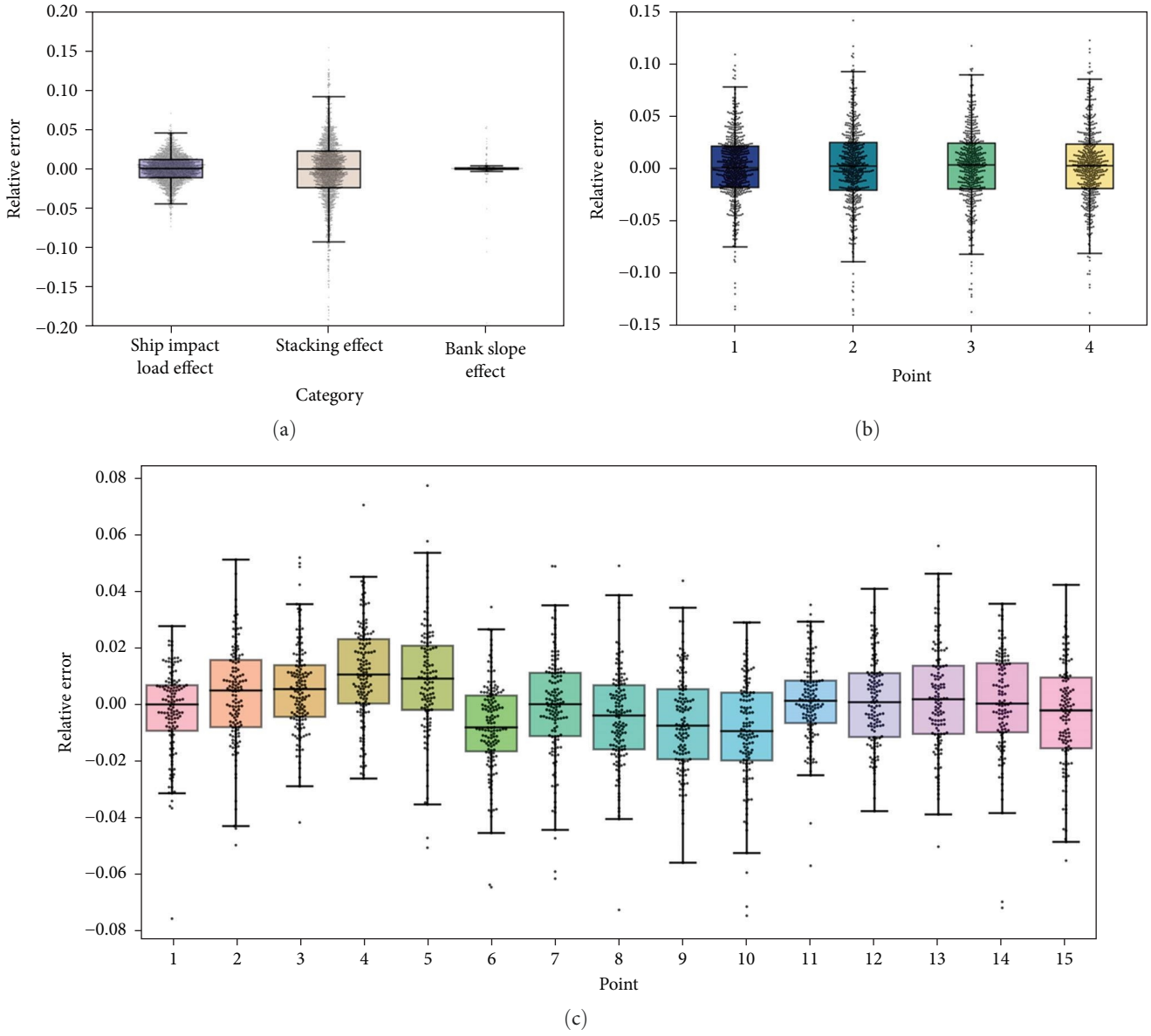

Figure 14: Regression model relative error plots: (a) types of damage inducements; (b) position of stacking loading; (c) position of ship impact load effect.

Table 7: Classification model test metrics.

Inversion category	Sample size	Precision rate	*F*1-score	Recall rate
Types of damage inducement effect	4,200	0.999	0.999	0.998
Location of damage inducement effect	4,000	0.975	0.978	0.976

reveals that the differences between the true and predicted values are less, and the kernel density curves exhibit good agreement.

5.4. Regression Test of the Inverse Model of the Intensity of DIF. The performance of the inverse model of effect strength on the sample test set is shown in Table 8. NSE, WI, R^2, and PBIAS coefficients—statistical parameters used to measure the degree of model fit—are introduced to examine the accuracy of the regression model from a variety of angles. The closer the last parameter is to 0 (indicating less model error) and the closer the first three parameters are to 1 (indicating a better fit).

Comparing Table 8 with Table 6, it can be seen that the MAE and MSE, although increased, still have small values. PBIAS is just 0.095, and the remaining four parameters [26]—R^2, NSE, WI, and 0.986, 0.986, and 0.996, respectively—show that the model's overall predictive tendency is

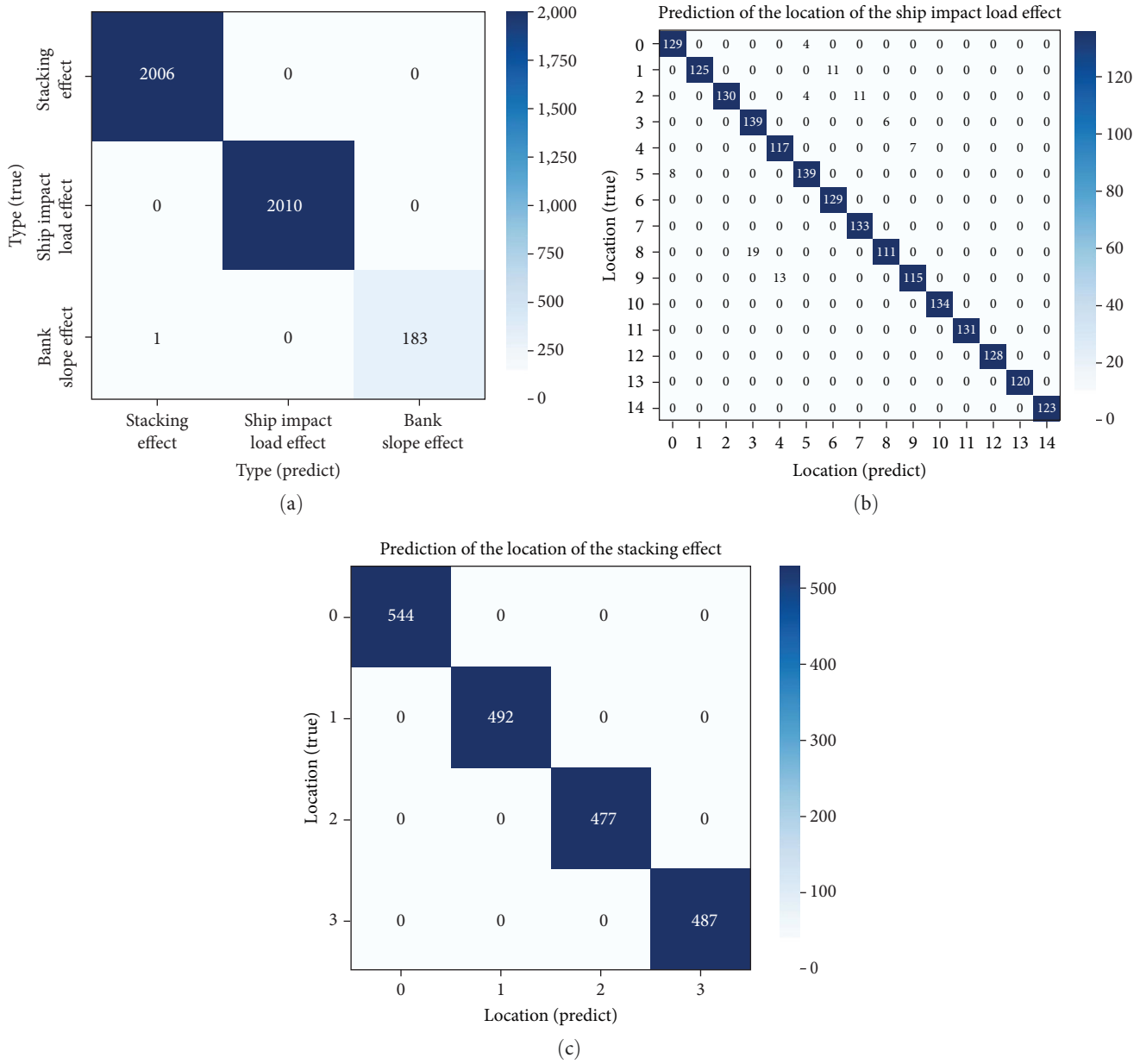

FIGURE 15: Inversion thermodynamic diagram of damage-inducing factor types and loading location: (a) types of damage-inducing factor; (b) position of ship impact load effect; (c) position of stacking loading.

excellent. This indicates that the inverse model for damage inducement strength prediction has high accuracy.

The box-and-line plot of the relative error under each injury causation category was extracted and plotted below.

Figure 14(a) shows that the ship striking action is anticipated with a moderate error of less than 5%, the bank slope action is predicted with less error, and the relative prediction error for the heap load action is close to 8% with fewer anomalies points.

In Figure 14(b), a box plot represents the relative errors of the strength prediction under each action point of the ship collision. Under the influence of ship collision, it is evident that the model's strength prediction error distribution at each action point is centralized, floating above and below the 0-point, and devoid of any clear skewness pattern. The relative error upper and lower boundaries are also less than 6%, and each action point only contains a very small number of prediction anomalies. The aforementioned illustrates how accurate and successful the PSO-SVM prediction model is in predicting the severity of ship collisions.

In Figure 14(c), a box plot represents the relative errors of the strength prediction under each action point of the stacking effect. Similar to the ship impact action, the stacking action error distribution exhibits more anomaly points, and

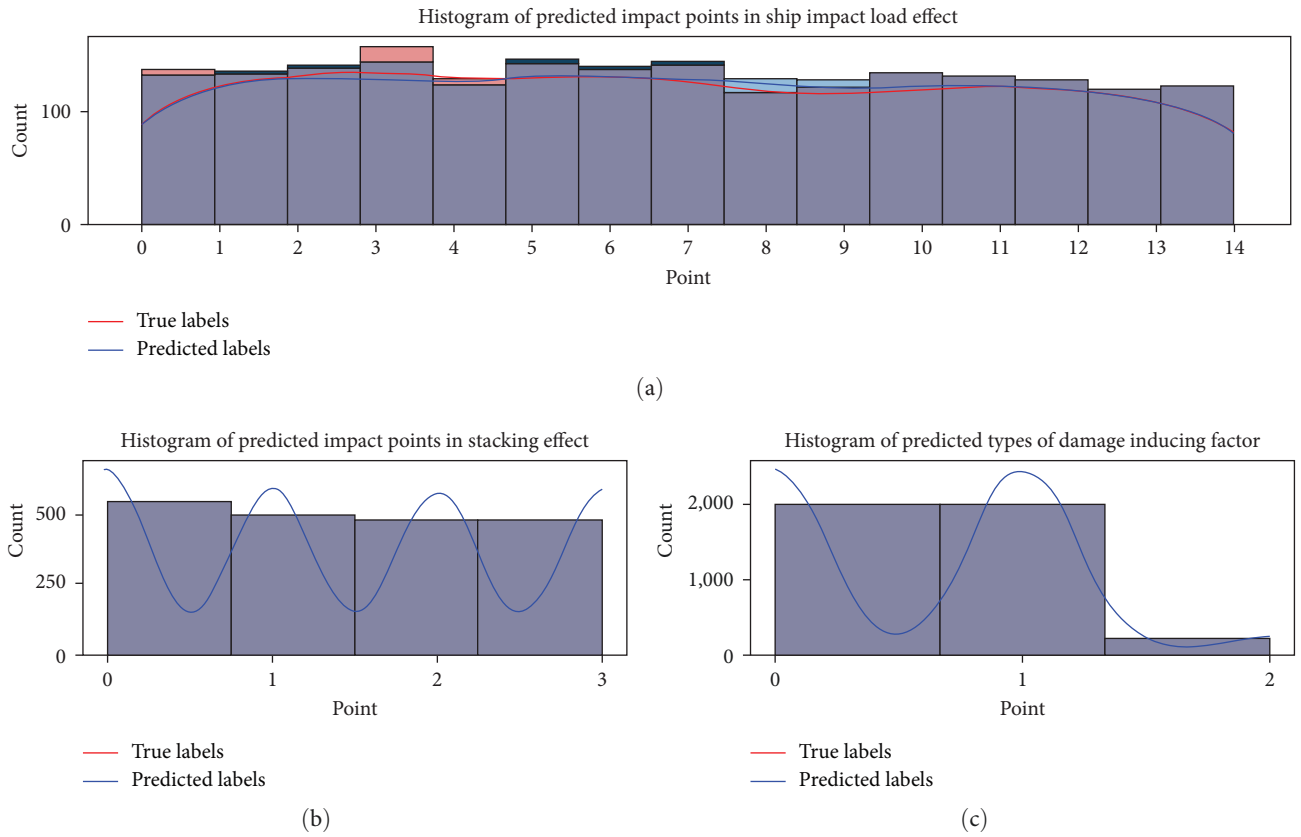

Figure 16: Histograms of damage inducement types and loading location: (a) position of ship impact load effect; (b) position of stacking loading; (c) types of damage inducements.

Table 8: Regression model test metrics.

Inversion category	Sample size	MAE	MSE	R^2	NSE	WI	PBIAS
Strength of damage-inducing factor	4,200	4.871	1.202	0.986	0.986	0.996	0.095

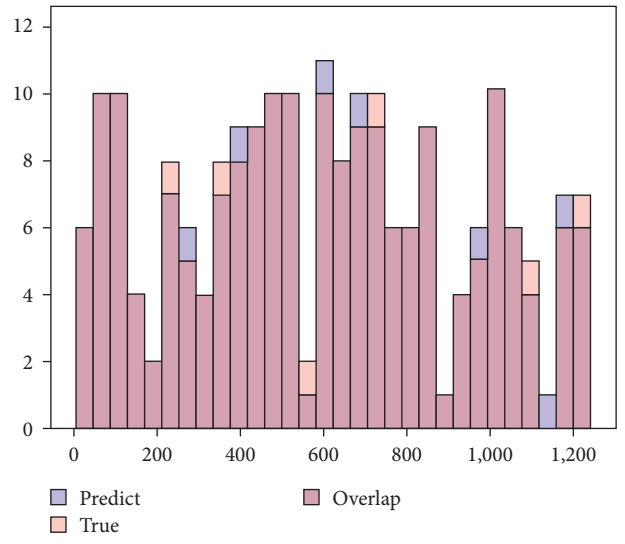

Figure 17: Histogram of stresses acting on the bank slope.

while the strength prediction may be impacted in certain instances, it is still very accurate in the great majority of situations.

Extract the predicted values of bank slope effect strength and plot the histogram with the true values as in Figure 17. The two data distributions are approximate and combined with Figure 14(a), which shows that the maximum relative error is only less than 2%, while there are very few anomalies.

To observe the fitting accuracy of the inverse model data more intuitively, 30 groups of damage inducements were randomly selected, respectively, and the prediction results of the three damage inducements were plotted as bar graphs after calculating the relative errors with the real effect strength, as shown in Figure 18. The largest relative error of the prediction results of the three damage inducements is only 7.87%.

In summary, the SVM optimized by particle swarm has high reliability in the inversion of damage inducement of overhead upright piers.

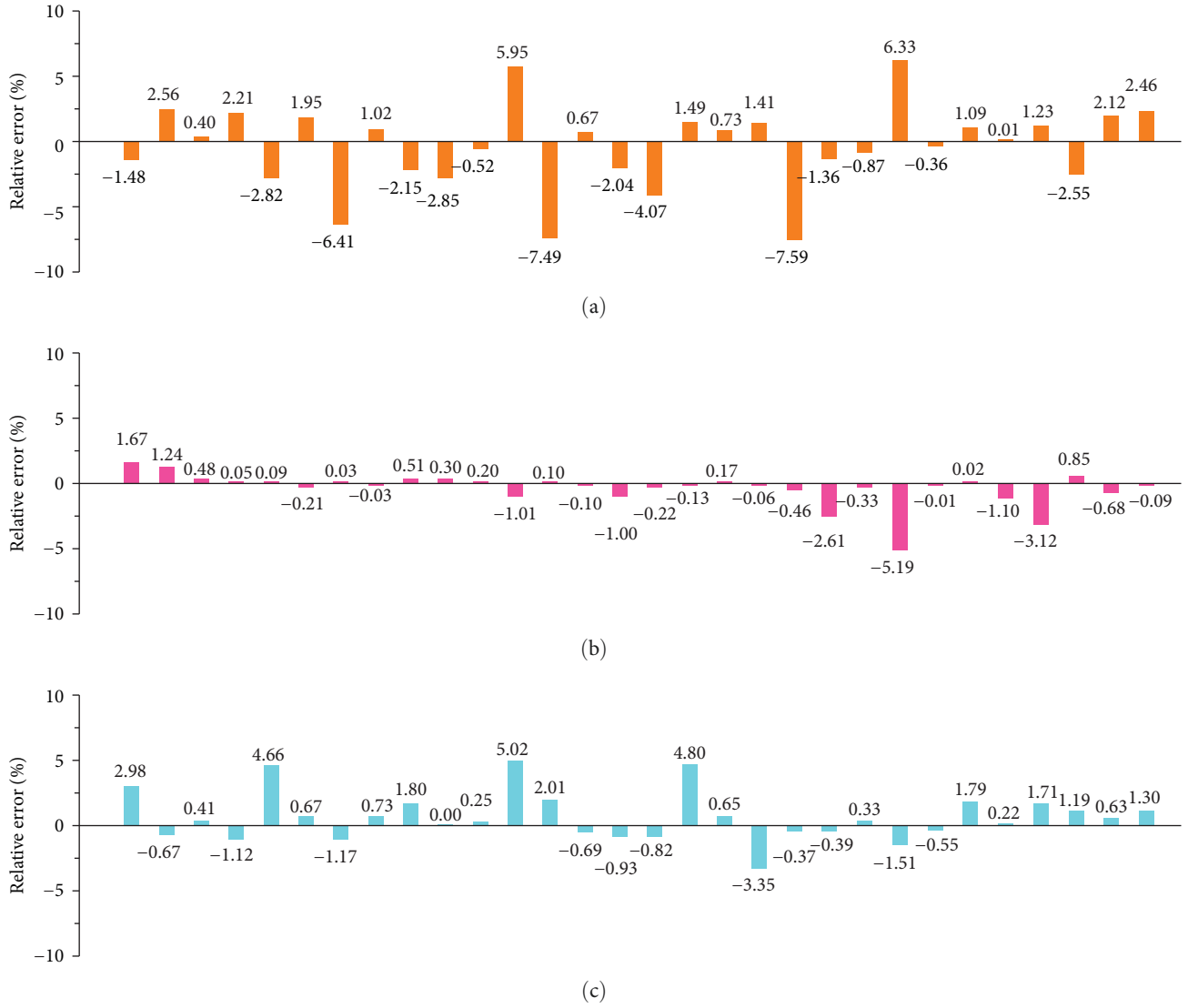

FIGURE 18: Random 30-group predictive relative error histogram for different damage inducements: (a) stacking effect strength; (b) bank slope effect; (c) ship impact load effect.

6. Conclusions

This research selects damage inducement as an important index for wharf monitoring and conducts damage inducement inversion research for the demand of real-time monitoring in the Xintian Port wharf.

The main findings are summarized as follows:

(1) For an overhead upright wharf, the finite element method was used to investigate the stress distribution characteristics of group piles under the influence of three different damage inducements. It was discovered that the stress distribution of group piles demonstrated blatant specificity under the influence of various damage inducements.

(2) By secondary development of abaqus through Python, 21,000 sets of stress data of group piles collected by different damage inducements are calculated and extracted. The types of damage causative factors, the location of the action, and the stress data are found to be correlated through the analysis of the stress data. A significant amount of redundant information is discovered by comparing the dimensions of the stress data; the sample set of the inversion model is constructed following the downscaling process of the stress data.

(3) A PSO-based damage causation inversion model for SVMs is presented.

The model's accuracy in predicting the kind and site of the injury-causing agent's action was 0.999, 0.975, and its corresponding $F1$ coefficients were 0.999, 0.978. The predicted values are extracted and plotted in heat maps and histograms, and it is discovered that the model has good accuracy, which satisfies the requirements of this study.

The introduced model evaluation parameters R^2, NSE, WI, and PBIAS are 0.986, 0.986, 0.996, and 0.095, respectively,

and the model's prediction results on the strength of the action mae and mse are 4.871 and 1.202, respectively. These metrics demonstrate the high reliability of the optimized inversion model. When the prediction results and errors are extracted to plot box line plots and histograms, it is evident that the maximum relative error of the shore slope action is 0.02, the maximum ship collision action is 0.05, and the stacking effect error is not greater than 0.08. This suggests that the model can accurately determine the degree of damage causative factors of the overhead upright wharf.

(4) This study included the bank slope action as a damage causative component by comparing the research in the same series [27–31]. By examining its correlation with the stress data, it was discovered that it has a significant impact on the stress data, which may raise the pier structure's risk. Based on this, a statistical analysis of the stress data demonstrated a clear association between the stress data and each damage causation parameter. The optimization method (PSO) was then incorporated to address the blind spot during the parameter adjustment process. Compared with the same type of study [29], after adding the bank slope thrust, the accuracy of the model strength prediction decreased slightly, but the species and location prediction improved slightly (previous model, strength R^2 0.994, species accuracy 0.98, location accuracy 0.975); this may be due to the difficulty of the model prediction due to the addition of the bank slope load, but thanks to the optimization of the PSO and the SVM's good classification power, there are better results in the identification of species and location ability. It makes the model have better results in species and location identification. In summary, the model could accurately identify the type and location of the damage causative agent, and at the same time inversely perform the corresponding intensity. In summary, the model could accurately identify the type and location of the damage causative agent, and at the same time inversely perform the corresponding intensity. The implementation of PSO results in a faster convergence speed, eliminating the need for manual parameter tuning and improving the accuracy of species and location identification. However, the addition of bank slope action somewhat reduces the accuracy of intensity prediction but still satisfies the objectives of this study.

6.1. Future and Prospects. An important direction for this topic in the future is to integrate the wharf monitoring data with numerical simulation and intelligent algorithms for multivariate data fusion to realize the long-term intelligent multivariate monitoring of the Xintian Port. The inversion of DIF of overhead vertical high pile wharf is a research topic of great practical significance. The results predicted by the inversion model are the important parameters of the digital twin model of Xintian Port Wharf, which is the important foundation of intelligent monitoring. As a result of the study's limitations—which include the intricacy of the research object and the realities of technical considerations—the following recommendations for further research are made:

The DIF used in this article are simplified loads, which are the design values extrapolated from the pertinent specifications and increased by 20%–50%. Future research will concentrate on the range of loads used in Xintian Port's real operations. The mechanical environment around the wharf itself is complicated; rather than focusing on a single load in this study, it is more common for many loads to occur simultaneously. Future studies will primarily focus on the inverse detection of various loads.

Data Availability

The data used to support the findings of this study are included within the manuscript.

Conflicts of Interest

The authors declare that there are no conflicts of interest.

Acknowledgments

This study was funded by the Chongqing Transportation Science and Technology Project (CQJT2022ZC03) Science and Technology Research Program of the Chongqing Education Commission of China (no. KJQN201800739).

Supplementary Materials

Supplementary 1. The raw data of the sample set.

Supplementary 2. Scripts for secondary development of finite element software for batch processing.

Supplementary 3. Support vector machine script.

References

[1] J. Wu, Y. J. Shu, S. L. Zhou, L. Y. Bai, and S. B. Cao, "Structure monitoring method and experiment of large-scale wharf bollards," *Optics and Precision Engineering*, vol. 29, no. 7, pp. 1631–1639, 2021.

[2] Y. J. Shu, J. Wu, and S. L. Zhou, "Identification of pile damage of high-piled wharf by fiber grating sensing array," *Optics and Precision Engineering*, vol. 29, no. 10, pp. 2349–2362, (in Chinese), 2021.

[3] Z. R. Xiang, Y. Wang, W. P. Qian, and Z. Y. Gu, "A method and experiment of rapid identification of time-varying load using limited vibration response," *Journal of Vibration and Shock*, vol. 41, no. 12, pp. 275–282, (in Chinese), 2022.

[4] C. H. Huang and Z. B. Wei, "Structural health monitoring of seaport wharf," *Port & Waterway Engineering*, vol. 04, pp. 106–109, (in Chinese), 2009.

[5] M. Zhao, G. Wu, and K. Wang, "Comparative analysis of dynamic response of damaged wharf frame structure under the combined action of ship collision load and other static loads," *Buildings*, vol. 12, no. 8, Article ID 1131, 2022.

[6] L. Q. Liu, J. F. Chen, C. Luo, and W. T. Hu, "Dynamic response and damage analysis of high-piled wharves under

ship impact," *Journal of Harbin Engineering University*, vol. 44, no. 4, pp. 519–526, 2023.

[7] D. Zhao, J. J. Wang, and S. Y. Huang, "Experimental study on influence of heaping on bending moment of frame wharf pile foundation," *Journal of Water Resources and Architectural Engineering*, vol. 17, no. 5, pp. 32–36, 2019.

[8] T. Shu, W. Tao, H. T. Lu, H. Li, J. X. Cao, and J. W. Ma, "A hybrid random forest and least squares support vector machine model based on particle swarm optimization algorithm for slope stability prediction: a case study in Sichuan-Tibet Highway, China," *Advances in Civil Engineering*, vol. 2023, Article ID 6651323, 20 pages, 2023.

[9] S. Wang, X. Sui, Y. Liu, H. Gu, B. Xu, and Q. Xia, "Prediction and interpretation of the deformation behaviour of high arch dams based on a measured temperature field," *Journal of Civil Structural Health Monitoring*, vol. 13, no. 2-3, pp. 661–675, 2023.

[10] M. J. Li, Y. Pan, Y. L. Liu, Y. Z. Wang, W. C. Zhang, and J. X. Wang, "Dam deformation forecasting using SVM-DEGWO algorithm based on phase space reconstruction," *PLoS One*, vol. 17, no. 6, Article ID e0267434, 2022.

[11] X. Zhang, Z. Y. Xu, H. R. He, and F. Wang, "Wind turbine blade cracking fault prediction based on RBM and SVM," *Power System Protection and Control*, vol. 48, no. 15, pp. 134–140, 2020.

[12] G. L. Wu, H. M. Yuan, Z. J. Song, F. B. Yang, B. Gao, and S. B. Li, "Fault diagnosis for power transformer based on rough set and multi-class support vector machine," *High Voltage Engineering*, vol. 43, no. 11, pp. 3668–3674, 2017.

[13] S. J. Mohammed, S. L. Zubaidi, N. Al-Ansari, H. M. Ridha, A. Dulaimi, and R. Al-Khafaji, "Application of metaheuristic algorithms and ANN model for univariate water level forecasting," *Advances in Civil Engineering*, vol. 2023, Article ID 9947603, 15 pages, 2023.

[14] H. Xie, J. Dong, Y. Deng, and Y. Dai, "Research and model prediction on the performance of recycled brick powder foam concrete," *Advances in Civil Engineering*, vol. 2022, Article ID 2908616, 14 pages, 2022.

[15] F. Yin, Y. Hao, T. Xiao, Y. Shao, and M. Yuan, "The prediction of pile foundation buried depth based on BP neural network optimized by quantum particle swarm optimization," *Advances in Civil Engineering*, vol. 2021, Article ID 2015408, 15 pages, 2021.

[16] Q. H. Xiao, C. M. Li, S. X. Lei et al., "Using hybrid artificial intelligence approaches to predict the fracture energy of concrete beams," *Advances in Civil Engineering*, vol. 2021, Article ID 6663767, 12 pages, 2021.

[17] W. J. Jia, T. Wen, D. Li et al., "Landslide displacement prediction of Shuping landslide combining PSO and LSSVM model," *Water*, vol. 15, no. 4, Article ID 612, 2023.

[18] T. Fei, Z. Anan, Y. Jie, and C. Lin, "Inversion analysis of rock mass permeability coefficient of dam engineering based on particle swarm optimization and support vector machine: a case study," *Measurement*, vol. 221, Article ID 113580, 2023.

[19] C. He, J. Xing, J. Li, Q. Yang, R. Wang, and X. Zhang, "A combined optimal sensor placement strategy for the structural health monitoring of bridge structures," *International Journal of Distributed Sensor Networks*, vol. 9, no. 11, Article ID 820694, 10 pages, 2013.

[20] G. L. Wang, Y. F. Li, and D. X. Bi, "Support vector networks in adaptive friction compensation," *IEEE Transactions on Neural Networks*, vol. 18, no. 4, pp. 1209–1219, 2007.

[21] H. B. Zhao and X. T. Feng, "Study on genetic-support vector machine in displacement back analysis," *Chinese Journal of Rock Mechanics and Engineering*, vol. 22, no. 10, pp. 1618–1622, (in Chinese), 2003.

[22] W. C. Huang, H. Y. Liu, Y. Zhang et al., "Railway dangerous goods transportation system risk identification: comparisons among SVM, PSO-SVM, GA-SVM and GS-SVM," *Applied Soft Computing*, vol. 109, no. C, 2021.

[23] A. R. Shooli, A. R. Vosoughi, and M. R. Banan, "A mixed GA-PSO-based approach for performance-based design optimization of 2D reinforced concrete special moment-resisting frames," *Applied Soft Computing*, vol. 85, Article ID 105843, 2019.

[24] J. Q. Chen and H. Y. Li, "Airfoil optimization of land-yacht robot based on hybrid PSO and GA," *International Journal of Pattern Recognition and Artificial Intelligence*, vol. 33, no. 13, 2019.

[25] H. G. Kim, K. H. Cho, and F. Recknagel, "Time-series modelling of harmful cyanobacteria blooms by convolutional neural networks and wavelet generated time-frequency images of environmental driving variables," *Water Research*, vol. 246, Article ID 120662, 2023.

[26] T. A. Demissie, "Impact of climate change on hydrologic components using CORDEX Africa climate model in Gilgel Gibe 1 watershed Ethiopia," *Heliyon*, vol. 9, no. 6, Article ID e16701, 2023.

[27] S. L. Zhou, C. R. Ke, F. Wu et al., "Inversion model of ship impact force of overhead vertical piers based on support vector machine," *Port & Waterway Engineering*, vol. 08, pp. 21–27, 2023.

[28] S. L. Zhou, C. Xiong, C. R. Ke et al., "Back analysis model of damage incentives of inland river overhead vertical wharf based on random forest," *Port & Waterway Engineering*, vol. 07, pp. 53–59, 2023.

[29] L. D. Zuo, *Research on Inversion Method of Damage Cause of Overhead Vertical Wharf in High Fill Area Based on Pile Stress*, Chongqing Jiaotong University, Chongqing, China, 2022.

[30] S. B. Cao, *Inversion Analysis of Damage Inducement of Overhead Vertical Wharf in Three Gorges Reservoir Area*, Chongqing Jiaotong University, Chongqing, China, 2021.

[31] X. C. Yang, *Under the Combined Action of Injury Inducements Inversion Analysis of Overhead Vertical Wharf*, Chongqing Jiaotong University, Chongqing, China, 2023.